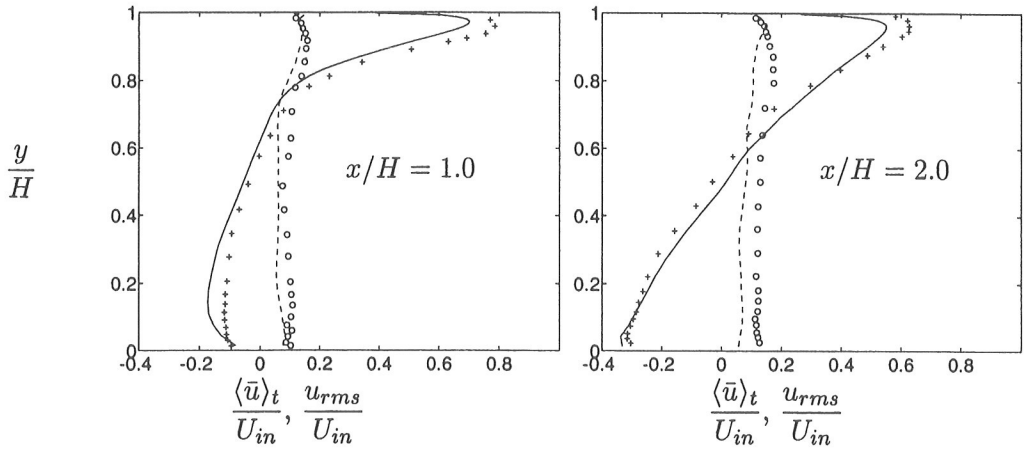

Figure 14. Time averaged velocity and resolved rms velocity profiles. $72 \times 42 \times 52$ mesh. Symmetry plane $z/H = 0.5$. LES using the dynamic model. Solid lines: $\langle \bar{u} \rangle_t / U_{in}$; dashed lines: u_{rms}/U_{in}; +: experimental mean velocity; *o*: experimental fluctuations.

are used to when using traditional eddy viscosity models where high turbulent viscosity is connected with flat, smeared-out velocity profiles.

Some longitudinal vortices are visible in Fig. 17b. It seems like the mesh is too coarse in the z-direction. Near the ceiling in the middle it looks like the flow is trying to form longitudinal vortices, but that the grid resolution is insufficient. From Table 2 we find that the maximum cell-size in the spanwise direction expressed in viscous units is $\Delta z_{max} u_* / \nu \simeq 150$. From experiments [34] and DNS-simulations [35] it is known that the width (diameter) of these longitudinal vortices, caused by alternating low- and high-speed streaks in the spanwise direction, is around 100 viscous units. Clearly the meshes used in the present work is too coarse to capture these phenomena. As noted by Piomelli [36], it may not be necessary to capture these effects if we only are interested in mean velocities and rms fluctuations.

In Fig. 18 zoomed views of vector plots in the upper-right and the lower-left corners are presented. The recirculation bubble near the ceiling is nicely captured. In the recirculation bubble near the floor the velocities are much smaller ($< 0.03 U_{in}$), and we can see three vortices.

The resolved $\bar{u}$ velocities versus time at four chosen points are presented in Fig. 19. It can be seen that the fluctuations in $\bar{u}$ are strong. In the middle of the room (Fig. 19b) it is not meaningful to define a "mean" velocity $\langle \bar{u} \rangle_t$, since $\bar{u}/U_{in}$ fluctuates between 0.15 and -0.23 and the time averaged velocity is close to zero. It can also be seen that the frequency of $\bar{u}$ is much higher in the wall jet near the ceiling (Figs. 19a,c) than in the back-flow region close to the floor (Fig. 19d). In addition to the large-scale fluctuations visible in Fig. 19 we have small-scale fluctuations which can be seen in Fig. 20. These small-scale fluctuations are generated by the inlet boundary conditions, where a randomized velocity field is prescribed (see Eq. 28). If constant flow conditions (in time) are prescribed, the small-scale fluctuations go away. Also the time history of the $\bar{u}$ velocities (like that shown in Fig. 19) becomes less chaotic.

In Fig. 21 the C coefficient in the dynamic model (see Eq. 17) is presented. Figure 21a shows the time history of C at two chosen points, one point in the wall jet close to the ceiling, and one point in the boundary layer close to the floor. The variation of C is fairly big, especially close to the floor where the amplitude of the fluctuations is larger than $\langle C \rangle_t$. It should be noted that at these two chosen

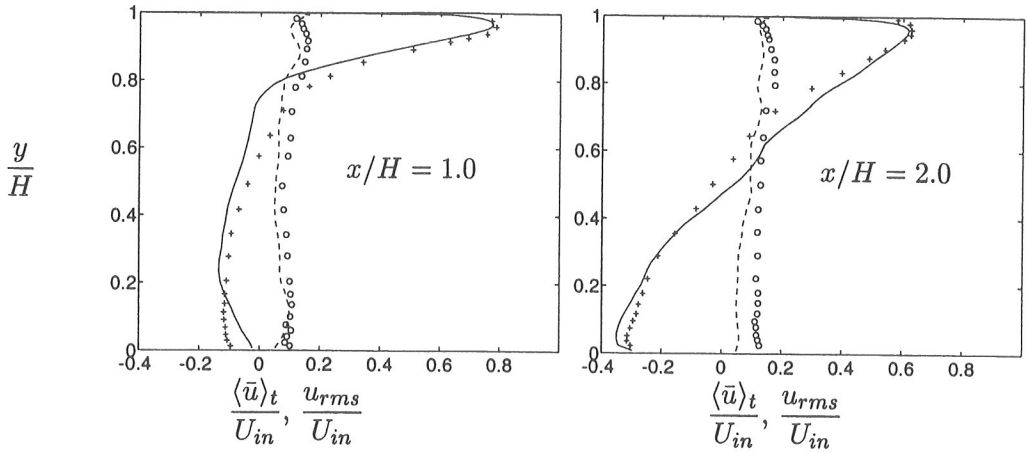

Figure 15. Time averaged velocity and rms velocity profiles. $102 \times 52 \times 52$ mesh. Symmetry plane $z/H = 0.5$. LES using the dynamic model. Solid lines: $\langle \bar{u} \rangle_t / U_{in}$; dashed lines: u_{rms}/U_{in}; +: experimental mean velocity; *o*: experimental fluctuations.

point it is only at $t \simeq 260$ that C goes negative. (As mentioned in the beginning of Sub-section 5.2.2 the total viscosity is not allowed to go negative.) In Fig. 21b the instantaneous C versus y is shown, and it can be seen that C is small at the floor and ceiling as it should. The average value of C in the y-direction is approximately 0.04 which in the Smagorinsky model corresponds to

$$C_S = \sqrt{C} = 0.2$$

The present values on C are smaller than those obtained by Zang *et al.* [16] and approximately two times larger than those found by Yang and Ferziger [33], which confirms that C is flow dependent.

The point of separation x_{sep} along the ceiling and the floor are shown in Fig. 22. The spanwise averaged values are shown (solid lines). The frequency of x_{sep} is similar to that of the velocity itself. The location of separation along the ceiling is fluctuating very much whereas it is more stable along the floor. In Fig. 16 the $\bar{u}$-velocities at the centerline along the ceiling ($y = H - h/2$) and the floor ($y = h/2$) are shown. The dotted lines in Fig. 22 show the x-location where those $\bar{u}$-velocities change sign versus time. It occurs both close to the ceiling and close to the floor that $\bar{u}$ does not change sign but that the flow continues all the way to the opposite wall. It happens only once close to the ceiling ($t \simeq 120$ in Fig. 22a) but several times close to the floor.

The two-point correlation coefficient $R_{u'',u''}(y, y_0)$ [37]

$$R_{u'',u''}(y, y_0) = \frac{\langle u''(y) u''(y_0) \rangle_t}{\sqrt{\langle (u''(y))^2 \rangle_t} \sqrt{\langle (u''(y_0))^2 \rangle_t}} \tag{29}$$

is shown in Fig. 23. Using the two-point correlation coefficient we can compute the integral length scale Λ from [37]

$$\Lambda = \int_{y_1}^{y_2} R_{u'',u''}(y, y_0) dy. \tag{30}$$

The integration limits are taken at the point y_0 and away from the wall, which means that for the points at $y/H = y_0/H = 0.92$ we have $y_1/H = 0.92$, $y_2 = 0$, and for the points at $y/H = y_0/H = 0.14$ we use $y_1/H = 0.14$, $y_2/H = 1.0$. The integral length scales for four points are given in Table 3.

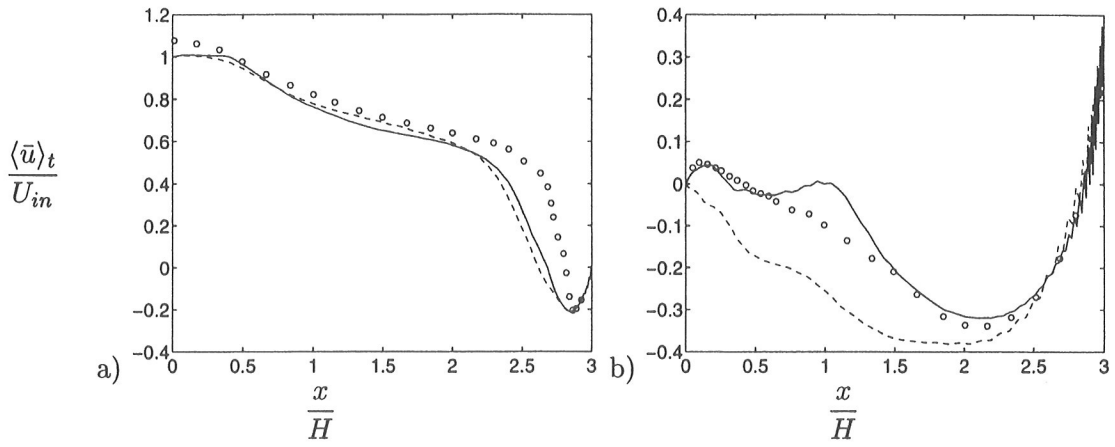

Figure 16. Time averaged $\bar{u}$ velocity along the ceiling and the floor. The dynamic model. $z/H = 0.5$. Solid line: $102 \times 52 \times 52$ mesh; dashed lines: $72 \times 52 \times 26$ mesh; o: experiments. a) $y = H - h/2$. b) $y = h/2$.

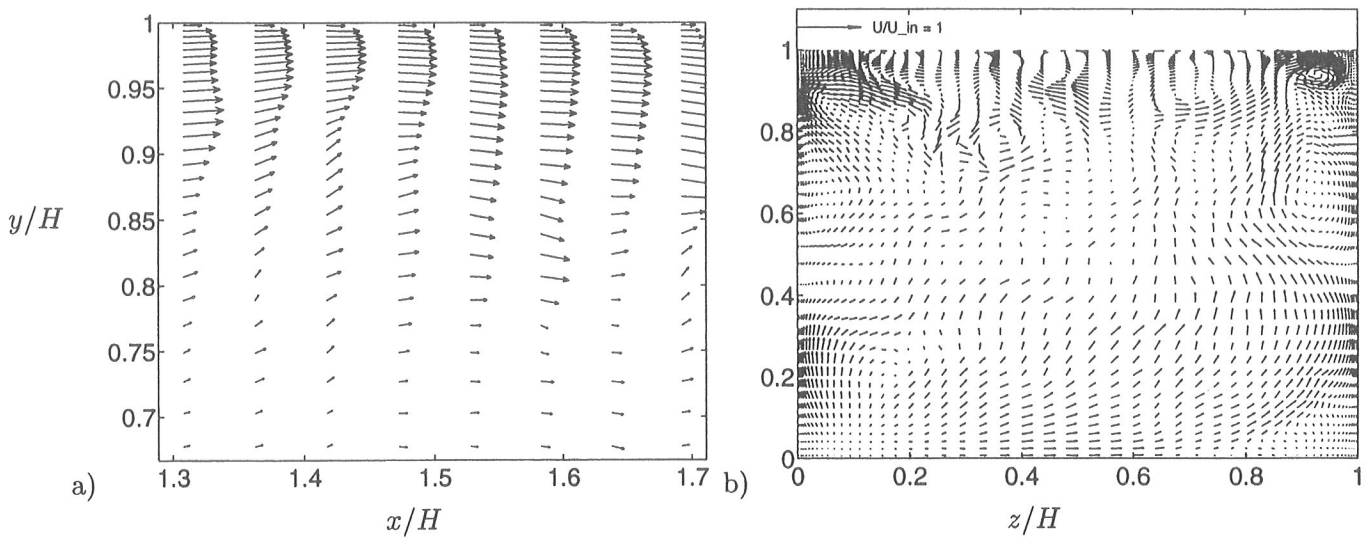

Figure 17. Velocity vectors at a given time. $102 \times 52 \times 52$ mesh. LES using the dynamic model. a) $z/H = 0.5$. b) $x/H = 1.5$.

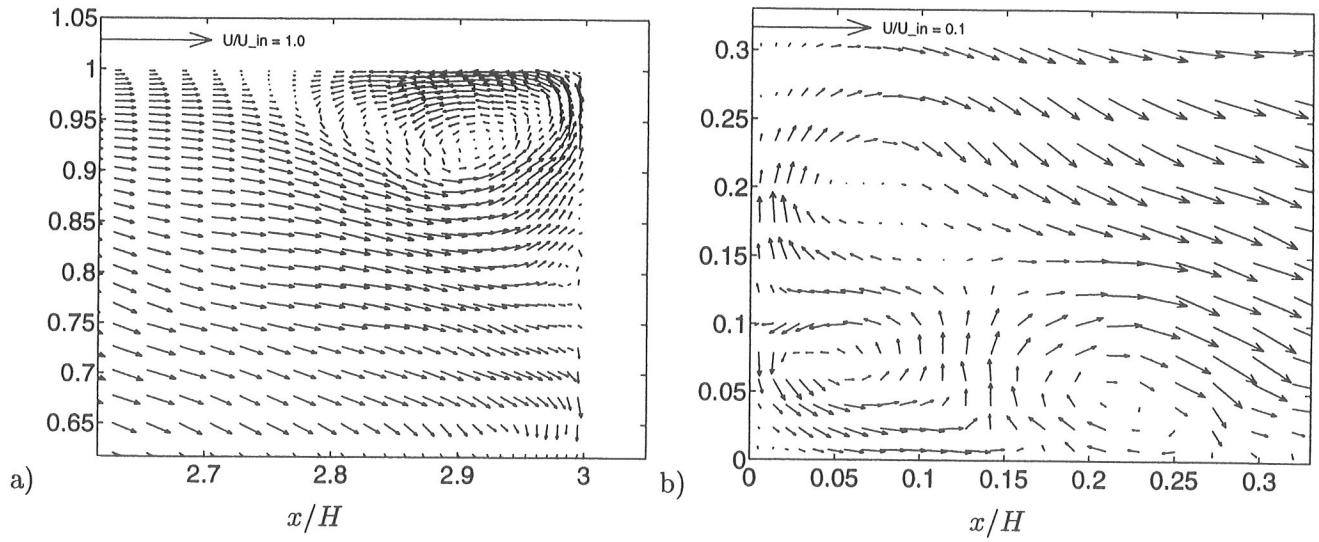

Figure 18. $102 \times 52 \times 52$ mesh. Instantaneous velocity vectors. $z/H = 0.5$. a) upper-right corner. b) lower-left corner.

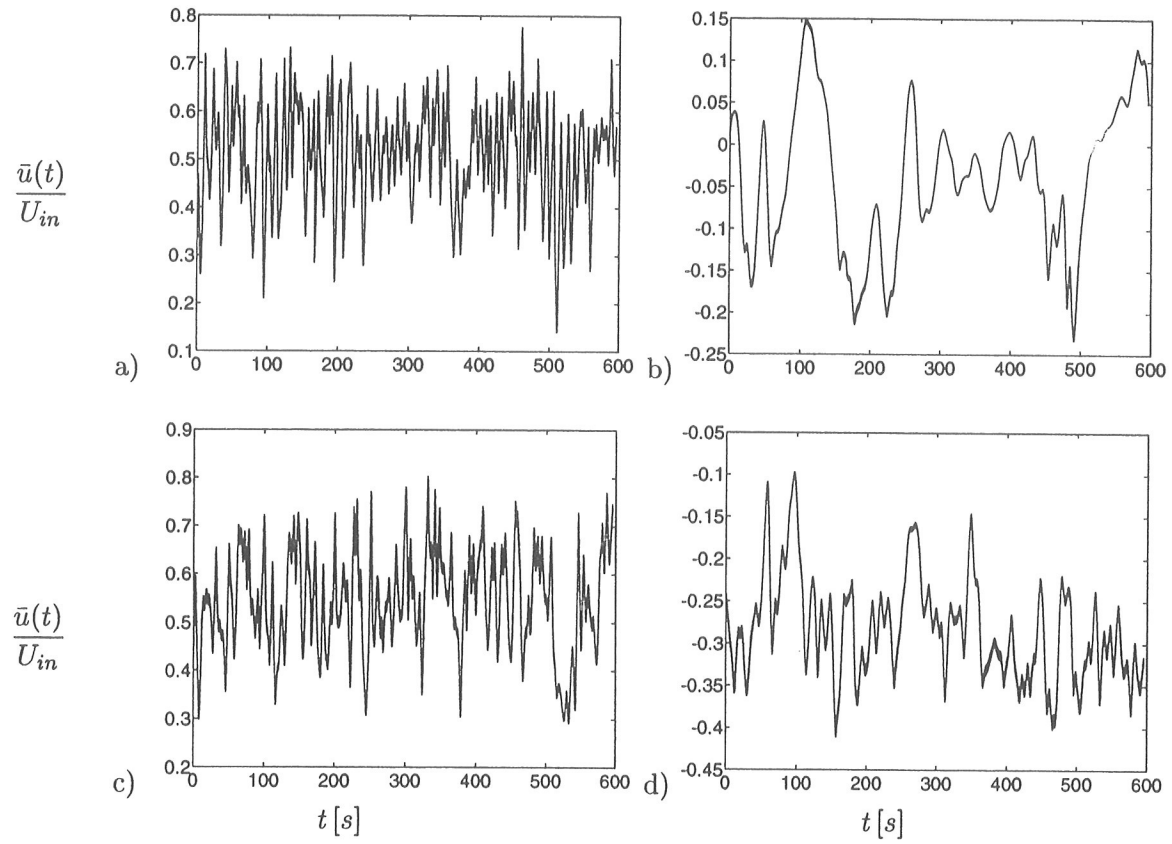

Figure 19. Time history of the $\bar{u}$ at four chosen cells. $72 \times 52 \times 26$ mesh. $z/H = 0.5$. Dynamic model. a) $x/H = 1.0, y/H = 0.92$, b) $x/H = 1.0, y/H = 0.5$, c) $x/H = 2.0, y/H = 0.92$, d) $x/H = 2.0, y/H = 0.14$.

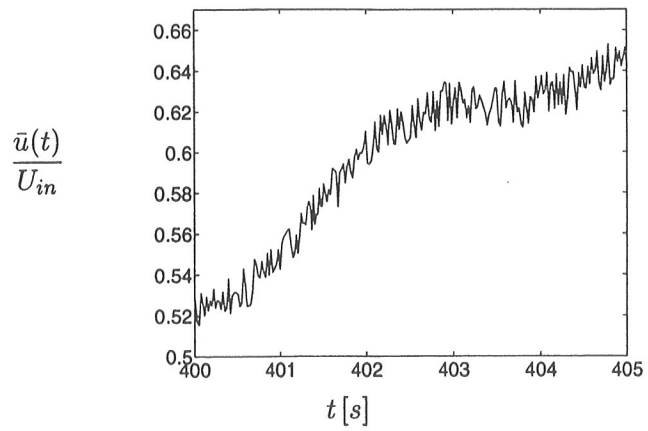

Figure 20. Time history of the $\bar{u}$ at $x/H = 2.0, y/H = 0.92, z/H = 0.5$ during a short time. $72\times52\times26$ mesh. Dynamic model.

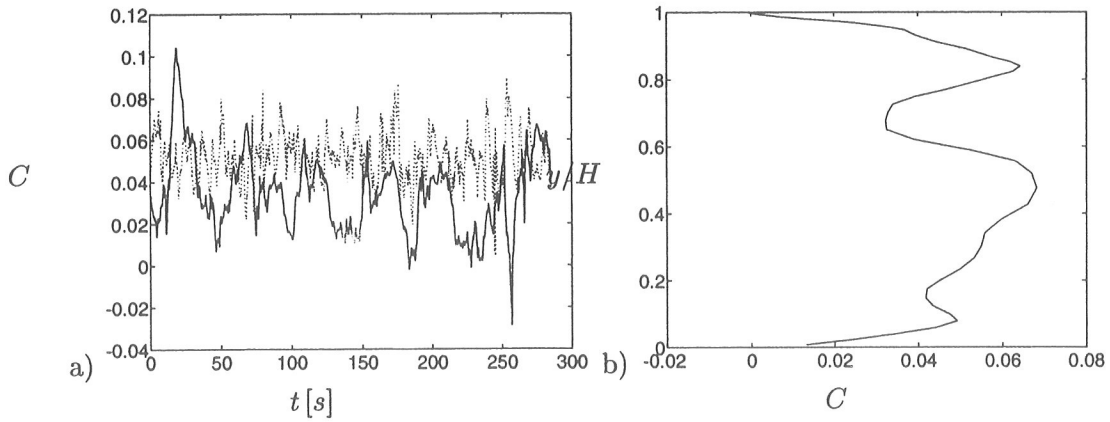

Figure 21. The C coefficient in the dynamic model. $x/H = 1.0, z/H = 0.5$. $102 \times 52 \times 52$ mesh. a) Time history of C at two points. Solid line: $y/H = 0.14$; dotted line: $y/H = 0.92$. b) Instantaneous vertical profile of C.

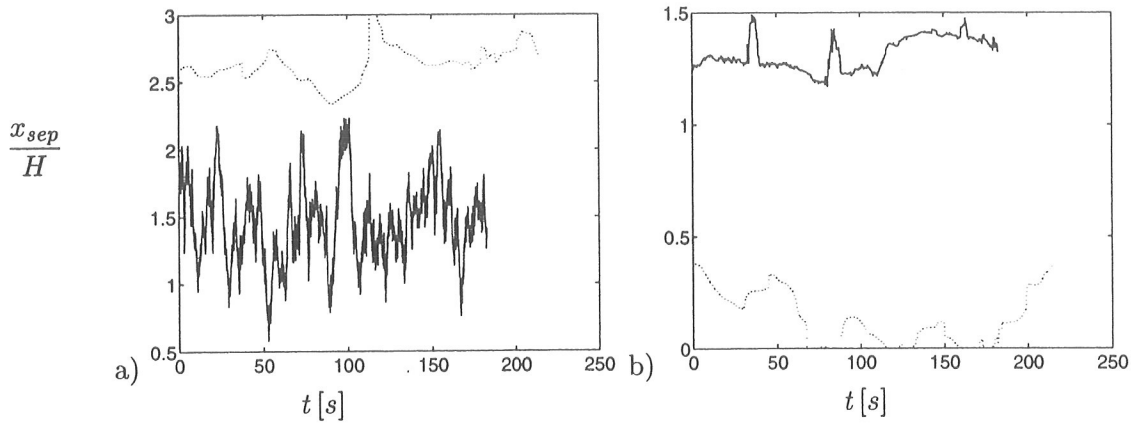

Figure 22. Solid line: spanwise averaged point of separation $\langle x_{sep}/H \rangle_z$; dotted line: point at the centerline $z/H = 0.5$ where $\bar{u}(n = h/2)$ changes sign. n denotes distance from ceiling and floor, respectively. $102 \times 52 \times 52$ mesh. a) Ceiling. b) Floor.

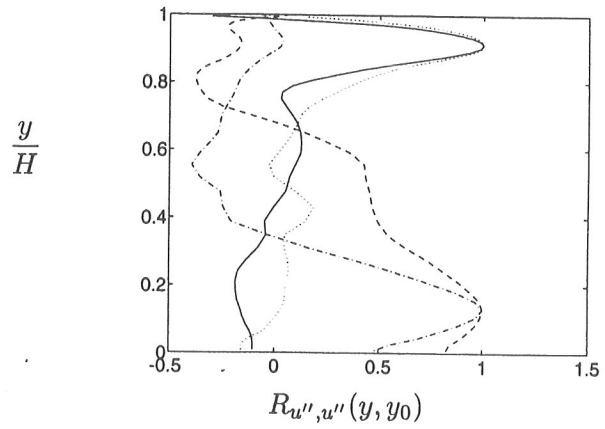

Figure 23. Two-point correlations $R_{u'',u''}(y, y_0)$. $72 \times 52 \times 26$ mesh. Dynamic model. Symmetry plane $z_0/W = 0.5$. Solid line: $x_0/H = 1.0, y_0/H = 0.92$; dotted line: $x_0/H = 2.0, y_0/H = 0.92$; dashed line: $x_0/H = 1.0, y_0/H = 0.14$; dash-dotted line: $x_0/H = 2.0, y_0/H = 0.14$.

The correlation coefficient for the two points in the wall jet at $x_0/H = 1.0$ and $x_0/H = 2.0$ are rather similar near the wall where the peak near the ceiling at $x_0/H = 2.0$ is slightly wider because the thickness of the wall jet is larger. However, the integral lengths are very different (see Table 3) because the negative tail in the $R_{u'',u''}(y, y_0)$ curve at $x_0/H = 1.0$ is much larger than at $x_0/H = 2.0$. This means that at $x_0/H = 1.0$ high $\bar{u}$ velocities in the wall jet are correlated with high negative $\bar{u}$ velocities close to the floor whereas this is not the case at $x_0/H = 2.0$. We find a similar difference for the two points close to the floor. The negative part of $R_{u'',u''}(y, y_0)$ is so strong at $x_0/H = 2.0$ that it almost annihilates the positive part of $R_{u'',u''}(y, y_0)$, which results in a integral length scale close to zero, see Table 3. The integral length scale at $x_0/H = 2.0$ is considerably larger mainly because there is good correlation between the $\bar{u}$ velocity close to the floor and the $\bar{u}$ velocity in the stagnant region up to $y/H \simeq 0.6$.

The probability density function of $\bar{u}$ is shown for four points in Fig. 24, two points in the wall jet and two points in the boundary layer close to the floor. For the points in the wall jet (Fig. 24a) the probability function show a preferred value of $\bar{u}$ showing that the flow has a well defined mean velocity and that the velocity is fluctuating around this mean value. Close to the floor (Fig. 24b) it is hard to find any preferred value of $\bar{u}$ which shows that the flow is irregular and unstable with no well defined mean velocity and large fluctuations.

In Fig. 25 the power density spectrum for the resolved streamwise fluctuation $(u'')^2$ is shown. In fully turbulent flow it should behave as $\Phi \propto n^{(-5/3)}$ (inertial region) which is included as a dashed line. We can see that there is some tendency to inertial region close to $f = 0.2$. This value agrees well with measurements by Sandberg [38]. The sharp decrease of Φ shows that the subgrid model is doing a good job in extracting energy from the resolved flow. The reason why we do not have any distinct inertial region in the spectra may well be connected to insufficient grid resolution. As mentioned on page 20, in connection with the discussion of Fig. 17b, the streamwise vortices in the wall jet region are not resolved properly.

6. Conclusions and Future Work

A numerical procedure for Large Eddy Simulations has been presented for prediction of recirculating flows. A simple Smagorinsky model and a dynamic model was tested. The following conclusions can

x_0/H	y_0/H	z_o/H	Λ_x/H	Λ_y/H	Λ_z/H
1.0	0.92	0.5	-	0.05	-
1.0	0.14	0.5	-	0.24	-
2.0	0.92	0.5	-	0.26	-
2.0	0.14	0.5	-	0.003	-
1.0	$1-h/(2H)$	0.5	0.29	-	-
2.0	$h/(2H)$	0.5	0.43	-	-
1.0	$1-h/(2H)$	0.5	-	-	0.014
2.0	$h/(2H)$	0.5	-	-	0.18

Table 3
Integral length scales.

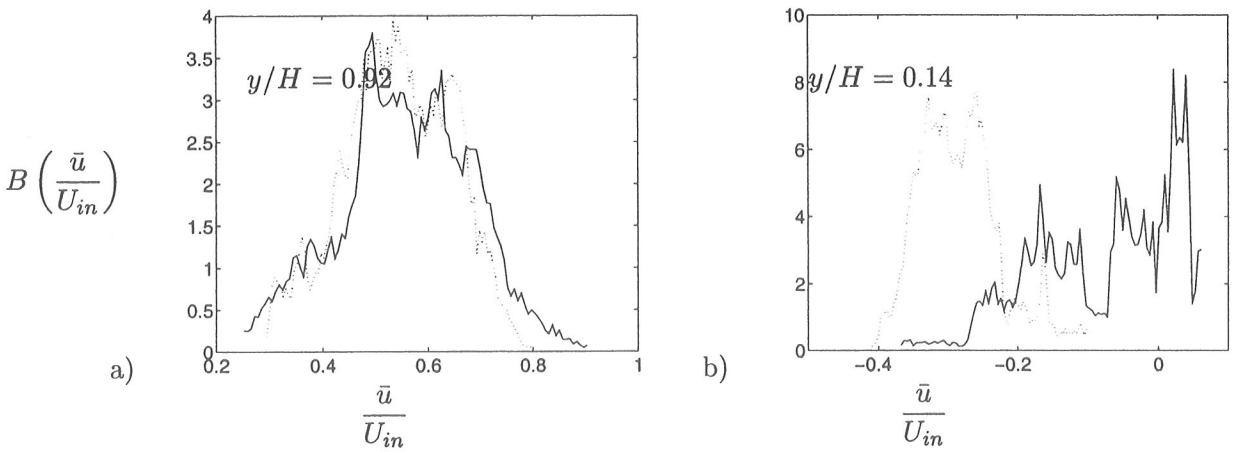

Figure 24. Probability density function of $\bar{u}$. $72 \times 52 \times 26$ mesh. The dynamic model. a) Solid line: $x/H = 1.0$; dotted line: $x/H = 2.0$. b) Solid line: $x/H = 1.0$; dotted line: $x/H = 2.0$;

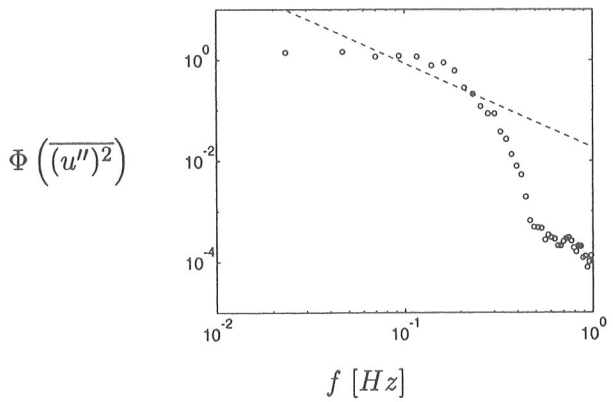

Figure 25. Power density spectrum $\Phi\left(\overline{(u'')^2}\right)$. $72 \times 52 \times 26$ mesh. Dynamic model. Symmetry plane $z/H = 0.5$. $x/H = 2.0, y/H = 0.92$.

be drawn:

- The simple Smagorinsky model was found to be inadequate, because the results were very dependent on the Smagorinsky-constant
- The pressure equation requires some 80 % of the total CPU-time
- The results obtained with the dynamic subgrid model gives results in good agreement with experiments

6.1. Future Work

In an ongoing work [39] we have found the multigrid solver solves the pressure equations more than 10 times faster on fine meshes (1 million nodes). We are also working on solving the whole equation system *implicitly* [39] using the same multigrid solver for the pressure. In the explicit method used in the present work the CFD-number must for stability reasons be below 0.4. With an implicit method the CFL-number is restricted only by concern of accuracy. Using CFL-number of one the implicit method is somewhat faster than the explicit method. If the CFL-number is allowed locally to exceed one (say 2), the implicit method gives a further speed-up of more than two.

REFERENCES

1. B.E. Launder and D.B. Spalding. The numerical computation of turbulent flows. *Computer Methods in Applied Mech. and Eng.*, 3:269–289, 1974.
2. M.M. Gibson and B.E. Launder. Ground effects on pressure fluctuations in the atmospheric boundary layer. *J. FluiD Mech.*, 86:491–511, 1978.
3. L. Davidson. Prediction of the flow around an airfoil using a Reynolds stress transport model. *ASME J. Fluid Engng.*, 117:50–57, 1995.
4. L. Davidson. Reynolds stress transport modelling of shock-induced separated flow. *Computers & Fluids*, 24:253–268, 1995.
5. B.E. Launder. Second-moment closure: Present ... and future? *Int. J. Heat and Fluid Flow*, 10:282–300, 1989.
6. M.A. Leschziner. Modelling engineering flows with Reynolds stress turbulence closure. *J. Wing Engng. and Ind. Aerodyn.*, 35:21–47, 1991.
7. K. Hanjalić. Advanced turbulence closure models: A view of current status and future prospects. *Int. J. Heat and Fluid Flow*, 15:178–203, 1994.
8. B.E. Thompson. Characteristics of a trailing-edge flow with turbulent boundary-layer separation. *Journal of Fluid Mechanics*, 157:305–326, 1985.
9. J. Smagorinsky. General circulation experiments with the primitive equations. *Monthly Weather Review*, 91:99–165, 1963.
10. M. Germano, U. Piomelli, P. Moin, and W.H. Cabot. A dynamic subgrid-scale eddy viscosity model. *Phys. Fluids A*, 3:1760–1765, 1991.
11. E.R. van driest. On turbulent flow near a wall. *J. Aero. Sci.*, 23:1007–1011, 1956.
12. P. Moin and J. Kim. Numerical investigation of turbulent channel flow. *J. Fluid Mech.*, 118:341–377, 1982.
13. W.P. Jones and M. Wille. Large Eddy Simulation of a jet in a cross-flow. In *10th Symp. on Turbulent Shear Flows*, pages 4:1 - 4:6, The Pennsylvania State University, 1995.
14. M. Germano, U. Piomelli, P. Moin, and W.H. Cabot. Erratum. *Phys. Fluids A*, 3:3128, 1991.
15. D.K. Lilly. A proposed modification of the Germano subgrid-scale closure method. *Phys. Fluids A*, 4:633–635, 1992.

16. Y. Zang, R.L. Street, and J.R. Koseff. A dynamic mixed subgrid-scale model and its application to turbulent recirculating flows. *Phys. Fluids A*, 5:3186–3196, 1993.
17. L. Davidson and B. Farhanieh. CALC-BFC: A finite-volume code employing collocated variable arrangement and cartesian velocity components for computation of fluid flow and heat transfer in complex three-dimensional geometries. Rept. 92/4, Thermo and Fluid Dynamics, Chalmers University of Technology, Gothenburg, 1992.
18. S.V. Patankar. *Numerical Heat Transfer and Fluid Flow.* McGraw-Hill, New York, 1980.
19. J. Kim and P. Moin. Application of a fractional-step method to incompressible Navier-Stokes equations. *J. Comp. Phys.*, 59:308–323, 1985.
20. F. Archambeau. *Large Eddy Simulation of Turbulent Vortex Shedding.* PhD thesis, UMIST, Dept. of Mech. Eng., Manchester, UK, 1995.
21. C.M. Rhie and W.L. Chow. Numerical study of the turbulent flow past an airfoil with trailing edge separation. *AIAA J.*, 21:1525–1532, 1983.
22. J. Renard and D. Gresser. Computational modelling of 2d hill flows. Diploma thesis. rept. 95/6, Thermo and Fluid Dynamics, Chalmers University of Technology, Gothenburg, 1995.
23. E. Blosch, W. Shyy, and R. Smith. The role of mass conservation in pressure-based algorithms. *Numer. Heat Transfer. Part B*, 24:415–429, 1993.
24. H. Le and P. Moin. Direct numerical simulation of turbulent flow over a backward facing step. Report no. TF-58, Stanford University, Dept. Mech. Eng., 1994.
25. Rodi W. *Turbulence Models and Their Application in hydraulics - a State of the Art Review.* International Association of Hydraulic Research, Monograph, Delft, 1984.
26. M. Wolfshtein. The velocity and temperature distribution in one-dimensional flow with turbulence augmentation and pressure gradient. *Int. J. Mass Heat Transfer*, 12:301–318, 1969.
27. H.C. Chen and V.C. Patel. Near-wall turbulence models for complex flows including separation. *AIAA J.*, 26:641–648, 1988.
28. B.P. Leonard. A stable and accurate convective modelling based on quadratic upstream interpolation. *Computational Methods in Applied Mechanical Engineering*, 19:59–98, 1979.
29. U. Ghia, K.N. Ghia, and T. Shin. High-Re solutions for incompressible flow using the Navier-Stokes equations and a multigrid method. *Comp. Phys.*, 48:387–411, 1982.
30. A. Restivo. *Turbulent Flow in Ventilated Rooms.* PhD thesis, University of London, Imperial College of Science and Technology, Mechanical Engineering Department, 1979.
31. P.V. Nielsen. Specification of a two-dimensional test case. Report, ISSN 0902-7513 R9040, Dept. of Building Technology and Structural Engineering,, Aalborg Universitetscenter, Aalborg, 1990.
32. B. van Leer. Towards the ultimate conservative difference scheme. Monotonicity and conservation combined in a second order scheme. *Journal of Computational Physics*, 14:361–370, 1974.
33. K.-S. Yang and J.H. Ferziger. Large-Eddy Simulation of turbulent obstacle flow using a dynamic subgrid-scale model. *AIAA J.*, 31:1406–1413, 1993.
34. S.J. Kline, W.C. Reynolds, F.A. Schraub, and P.W. Runstadler. The structure of turbulent boundary layers. *J. Fluid Mech.*, 30:741–773, 1967.
35. J. Kim, P. Moin, and R. Moser. Turbulence statistics in fully developed channel flow at low Reynolds number. *J. Fluid Mech.*, 177:133–166, 1987.
36. U. Piomelli. High Reynolds number calculations using the dynamic subgrid-scale stress model. *Phys. Fluids A*, 5:1484–1490, 1993.
37. J.O. Hinze. *Turbulence.* McGraw-Hill, New York, second edition, 1975.
38. M. Sandberg. Velocity characteristics in mechanically ventilated ofice rooms. In *ROOMVENT -87*, volume 2a, Stockholm, 1987.
39. P. Emvin and L. Davidson. Development and implementation of a fast Large Eddy Simulations method. Report (in press), Thermo and Fluid Dynamics, Chalmers University of Technology,

Gothenburg, 1996.